MODELING AND SIMULATION RESULTS ON A NEW COMPTON SCATTERING TOMOGRAPHY

Gaël Rigaud[1], M.K. Nguyen[1], T.T. Truong[2]

[1]Laboratoire Équipes Traitement de l'Information et Systèmes
CNRS UMR 8051/University of Cergy-Pontoise
6 avenue du Ponceau, 95014 Cergy-Pontoise Cedex, France
[2]Laboratoire de Physique Théorique et Modélisation
CNRS UMR 8089/University of Cergy-Pontoise
2 rue Adolphe Chauvin, 95302 Cergy-Pontoise Cedex, France
gael.rigaud@ensea.fr(Gaël Rigaud)

Abstract

Conventional tomography (X-ray scanner, Computed Tomography : CT, Single Photon Emission CT : SPECT,...) is widely used in numerous fields such as medical imaging and non-destructive testing. In theses tomographies, a detector rotates in space to collect primary radiation emitted by an object under investigation. In this case Compton scattered radiation behaves as noise hindering image quality and consequently correction to scatter should be applied. However recently an interesting new imaging concept, which uses precisely scattered radiation as imaging agent, has been advocated. The camera records now images labeled by scattered photon energy or equivalently scattering angle. Then it is shown that the three dimensional image reconstruction from scattered radiation data is feasible [1, 2, 3, 4, 5]. In this work we propose a new form of Compton scattering tomography (CST), akin to the X-ray scanning tomography, in the sense that it works in transmission but uses Compton scattered radiation. The new image formation modeling is based on a new class of Radon transforms on circular arcs. Through simulation results we show the feasibility and the relevance of this new process.

Keywords: Radon transforms (RT), Circular-arc Radon transform (CART), image reconstruction, Biomedical and nuclear imaging modeling, Compton scattering tomography (CST), scattered radiation

Presenting Author's Biography

Gaël Rigaud, M.Sc., is a 2010 graduate of the École Nationale Supérieure de l'Électronique et de ses Applications, France. He is presently working on a research project at ETIS under the supervision of Professor M.K. Nguyen. His research interest is in the field of modeling and simulation of Compton scattering tomography, inverse problems and generalization of Radon transform.

1 Introduction to Compton Scaterring Tomography (CST) and circular Radon transform

For more than fifty years, transmitted penetrating radiation such as X- or gamma-rays have been routinely used to probe the hidden parts of matter and/or tissues [6, 7, 8]. The measurement of their attenuation along all possible linear paths in a plane forms a set of Radon data, which, once fed into a chosen inversion formula, provides the reconstruction of the probed medium. In this imaging modality, scattered radiation acts as a nuisance blurring images and it should be removed or at least be compensated.

However it was realized, in the earlier seventies, that the Compton effect may give rise to new challenging imaging modalities.

Let us recall that the Compton effect (Fig. 1) is the scattering of X- or gamma-photons with electric charges.

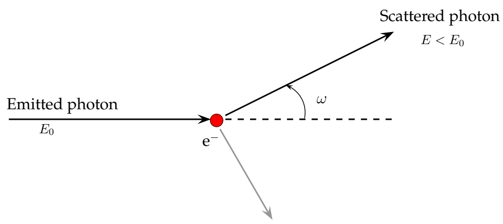

Fig. 1 Principle of Compton scattering

The energy of a scattered photon is related to the scattering angle ω by the Compton relation :

$$E = \frac{E_0}{1 + \frac{E_0}{mc^2}(1 - \cos\omega)} \tag{1}$$

where E_0 is the emitted photon energy and mc^2 represents the energy of an electron at rest (0.511 MeV).

The idea is to register the outgoing scattered photons according to their energies in order to image the hidden part of objects of interest. This is the basic idea in Compton scattering tomography (CST).

In 1994, S.J. Norton [9] worked out a CST modality which is based on a Radon transform on circles having a fixed common point. The functioning principle is given by Fig. 2. A point source **S** emits primary radiation towards an object, of which **M** is a scattering site (running point).

A point detector **D** moves along an *Ox*-axis and collects, at given energy E, scattered radiation from the object. The physics of Compton scattering demand that the registered radiation flux density g at site **D** is due to the contribution of all scattering sites **M** lying on an arc of circle from **S** to **D** subtending an angle $(\pi - \omega)$, where ω is the scattering angle corresponding to the outgoing energy E, as given by the Compton formula (equation (1)).

Norton gave the expression of the projections g as :

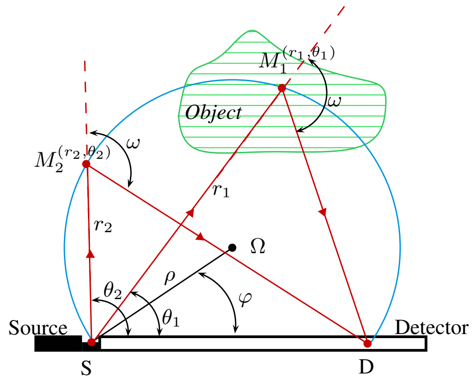

Fig. 2 Principle of Norton's CST

$$g(\rho,\varphi) = \int_0^{\pi} d\theta \int_0^{\infty} dr\, f(r,\theta)\, w(r,\theta;\rho,\varphi) \times\ \delta\left[r - 2\rho\cos(\theta-\varphi)\right] \tag{2}$$

where $\delta(.)$ is the 1-D Dirac delta function and $w(.)$ is defined by:

$$w(r,\theta;\rho,\varphi) = \frac{a\, r\, s(\theta)\, P(\omega)}{4\pi\,(2\rho)^3\,\sin^2\theta}\,. \tag{3}$$

In the above equation, a represents the area of an element of detection, $s(\theta)$ expresses any angular dependance of the γ-ray source distribution, and $P(\omega)$ (where $\omega = \pi/2 + \varphi$) is the Klein-Nishina differential cross section. Mathematically, g is essentially the Radon transform of the object electron density $f(M)$ on arcs of circle, when radiation attenuation and photometric effects on radiation propagation are neglected.

Norton proposed an inverse formula given by:

$$f(r,\theta) = \frac{1}{\pi^2}\int_0^{2\pi} d\varphi \int_0^{\infty} \rho\, d\rho\, \frac{g(\rho,\varphi)}{w(r,\theta;\rho,\varphi)} \times\ h\left[r - 2\rho\cos(\theta-\varphi)\right] \tag{4}$$

where

$$h(x) = \int_{-\infty}^{\infty} e^{-i\zeta x}\,|\zeta|\,d\zeta\,. \tag{5}$$

This expression is the same convolution kernel employed in the filtered Back-Projection algorithm used in x-ray transmission CT. The difference is that the Back-Projection is performed along straight lines in transmission CT, whereas here the Back-Projection is performed around the circles $r = 2\rho\ \cos(\theta - \varphi)$.

However the integral on the right of equation (5) should be interpreted as a distribution, since the integral does not converge. That's why Norton proposed an "apodization" function $A(\zeta)$ which goes to zero smoothly beyond the spatial-frequency cutoff (indeed the function $f(r, \theta)$ is bandlimited) and placed it under the integral.

$$h(x) = \int_{-\infty}^{\infty} A(\zeta)\, e^{-i\zeta x}\, |\zeta|\, d\zeta \,. \tag{6}$$

Recently we have suggested a novel modality for Compton scattering tomography. The physical principle is similar to Norton's CST, however in our configuration the source is not fixed but rotates around the object in order to collect more scattered photons.

Section 2 shows how image formation process in the new CST is modeled and how the collected data leads to a Radon transform on a particular class of circular arcs called Circular-Arc Radon transform (CART).

In section 3 we present numerical simulations on image formation and reconstruction including a point object and a Shepp-Logan phantom to support the feasibility of the new CST. The paper ends with a short conclusion on the obtained results and opens some future research perspectives.

2 Modeling of the new modality in Compton scattering tomography

First the modeling of image formation is presented. This leads to a novel Circular-Arc Radon transform (CART). Image reconstruction is then based on the analytical inversion formula of the CART and its corresponding Back-Projection inversion. The last form offers the advantage of reconstruction simulations by fast algorithms.

2.1 Modeling of formation image process and the Circular-Arc Radon transform (CART)

Consider a 2D-object represented by a non-negative continuous function $f(r, \theta)$ with bounded support. Fig. 3 shows how this modality of Compton scattering tomography works. An emitting radiation point source **S** is placed at a distance $2p$ from a point detector **D**. We consider only the upper part of the object. This is possible because an angle collimator is placed at **D**. The segment **SD** rotates around its middle **O** and its angular position is given by φ.

Emitted photons are scattered and some of them are detected by the detector **D** at an energy E_ω. So the detector can monitor scattered photons according to scattered energy which is related to the scattering angle by the Compton formula. Thus, for a fixed φ, to each energy E_ω corresponds a set of scattering sites on a circular-arc $C(\varphi, \omega)$.

Finally the detected radiation flux density $g(\varphi, \omega)$ is proportional to the integral of the electron density $f(M)$ with $\mathbf{M} \in C(\varphi, \omega)$. It can be written as

$$g(\varphi, \omega) = \int_{(r,\theta) \in C(\varphi,\omega)} f(r, \theta) ds \tag{7}$$

where ds is the elementary length of circular-arc to be computed from the circular arc equation

$$r = p(\sqrt{1 + \tau^2 \cos^2 \gamma} - \tau \cos \gamma) \tag{8}$$

where $\tau = \cot \omega$ and $\gamma = \theta - \varphi$. Thus

$$\tilde{g}(\varphi, \tau) = \int_{-\frac{\pi}{2}}^{\frac{\pi}{2}} f(r(\gamma), \gamma + \varphi)\, r(\gamma) \times \frac{\sqrt{1+\tau^2}}{\sqrt{1 + \tau^2\ \cos^2(\gamma)}} d\gamma \,. \tag{9}$$

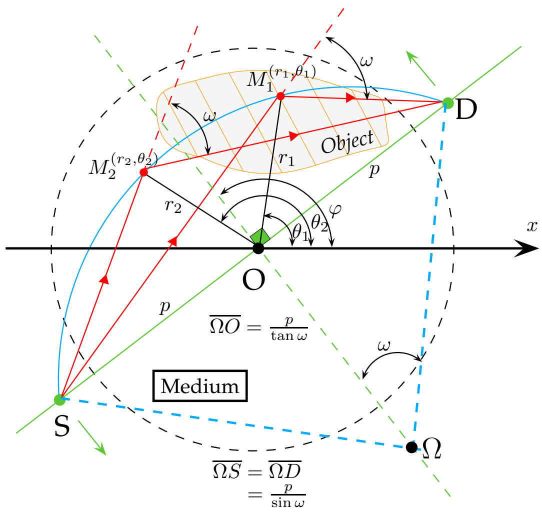

Fig. 3 Principle of the new CST based on the CAR transform

2.2 The inverse transform of the CART

The inverse transform can be worked out using the A.M. Cormack's technique [10] using Fourier angular components of f et g :

$$\begin{cases} f(r, \theta) = \sum_l f_l(r) e^{il\theta} \\ \text{with} \\ f_l(r) = \dfrac{1}{2\pi} \displaystyle\int_0^{2\pi} f(r, \theta) e^{-il\theta} d\theta \end{cases} \tag{10}$$

and

$$\begin{cases} \tilde{g}(\varphi, \tau) = \sum_l \tilde{g}_l(\tau) e^{il\varphi} \\ \text{with} \\ \tilde{g}_l(\tau) = \dfrac{1}{2\pi} \displaystyle\int_0^{2\pi} \tilde{g}(\varphi, \tau) e^{-il\varphi} d\varphi \end{cases} \tag{11}$$

Equation (9) now takes the form

$$\tilde{g}_l(\tau) = 2 \int_0^{\frac{\pi}{2}} r(\gamma) \frac{\sqrt{1+\tau^2}}{\sqrt{1+\tau^2 \cos^2(\gamma)}} \times f_l(\gamma) \cos(l\gamma) d\gamma \,. \tag{12}$$

Applying the inversion procedure of Cormack, we obtain the inverse formula [11]

$$f_l(r) = (-) \frac{2p(p^2+r^2)}{\pi(p^2-r^2)^2} \times \left[\frac{d}{dt} \int_t^{\infty} \frac{\cosh(l \cosh^{-1}(\frac{q}{t}))}{q\sqrt{(\frac{q}{t})^2 - 1}} \frac{\tilde{g}_l(\frac{1}{q})}{\sqrt{1+q^2}} dq \right]_{t=\frac{2pr}{p^2-r^2}} \tag{13}$$

where $q = 1/\tau$. Finally $f(r, \theta)$ is reconstructed through its Fourier expansion with the circular components $f_l(r)$.

3 Numerical analysis and simulation results

As an illustration of the feasibility of the new CST, we carried out numerical simulations on formation and on image reconstruction for two original objects : a point object and a Shepp-Logan medical phantom.

The scattering medium is discretized with NxN pixels. We consider the number of rotation N_φ and the number of energy levels N_ω. These numbers define the corresponding angular sampling step $d\varphi$ and $d\omega$ by :

$$d\varphi = \frac{2\,\pi}{N_\varphi} \quad \text{and} \quad d\omega = \frac{\pi}{2N_\omega} \tag{14}$$

Indeed $\omega \in]0, \frac{\pi}{2}]$ and $\varphi \in [0, 2\pi]$.

In order to have a "well-conditioned" problem, the number of projections ($N_\varphi \times N_\omega$) must be larger than the number of studied points ($N \times N$ here).

3.1 Image formation and the Circular-Arc Radon transform

For fixed (φ, ω), we calculate the set of points (x, y) on the circular-arc $C(\varphi, \omega)$ (equation (8)). Then to get $g(\varphi, \omega)$ (or projections), we multiply $f(x, y)$ by a differential element (equation (9)) and sum over pixels along the circular arc $C(\varphi, \omega)$. Fig. 4 shows how we scan the object to simulate measurements.

For small values of ω ($\omega \approx 0$), the scanning of the circular-arc becomes hard. According to the sampling rate $d\theta$, we can define an angle ω_0, below which we cannot get all the points of the circular-arc. This is why the area under the circular-arc $C(\varphi, \omega_0)$ is "ill-observed" hence "ill-reconstructed". Numerically we

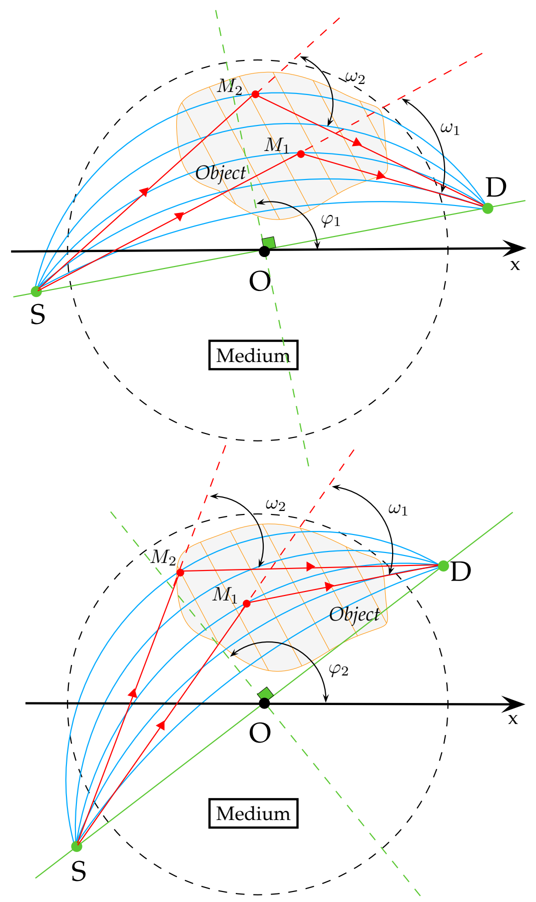

Fig. 4 Scanning of the medium

can reduce this phenomenon by decreasing $d\theta$ but at the expense of the computational time.

For a single point object, the response of the CAR transform (called the Point Spread Function : PSF) is given by the equation :

$$\omega = arctan \left(\frac{2pr}{p^2 - r^2} \cos(\theta - \varphi) \right) \,. \tag{15}$$

This equation can be established using the circular-arc equation (8) and express $\omega(\varphi)$ for a fixed point (r, θ) as a function of φ. Fig. 6 shows the shape of the $\arctan$ function which characterizes the CART of the point object.

3.2 Numerical analysis of the analytical inversion formula

The inversion formula (equation (13)) presents numerous difficulties for numerical implementation.

Indeed by studying the behavior of g when q tends towards ∞ for bounded f, we could show that it is equivalent to :

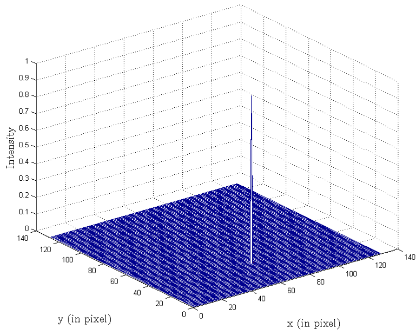

Fig. 5 Three-dimensional representation of a point object

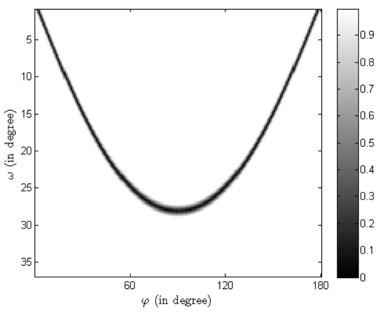

Fig. 6 CAR transform (PSF) of the point object in Fig. 5

$$\lim_{q\to\infty} \frac{\cosh(l\ \cosh^{-1}(\frac{q}{t}))}{q\sqrt{(\frac{q}{t})^2-1}} \approx \lim_{u\to\infty} 2\ e^{(l-2)u} \qquad (16)$$

Thus when $l > 2$, the function to integrate of equation (13) diverges. The implementation of the analytical inverse CART will be the subject of future work. This is why we use another way to reconstruct the studied medium : the Back-Projection method.

3.3 Inversion method by Filtered Back-Projection (FBP)

Let us recall the classical Radon transform which is defined as integral of object function on straight lines. The direct Radon transform is:

$$g(u,\varphi) = \int_{\mathbb{R}^2} dxdy\ f(x,y)\ \delta\left(u - x\cos\varphi - y\sin\varphi\right) \qquad (17)$$

and its inverse transform is:

$$f(x,y) = \frac{-1}{2\pi^2}\int_0^{\pi} d\varphi \int_{-\infty}^{+\infty} du \frac{g(u,\varphi)}{(u - x\cos\varphi - y\sin\varphi)^2} \qquad (18)$$

Equation (18) can be written as :

$$f(x,y) = \int_0^{\pi} d\varphi \int_{-\infty}^{+\infty} du \int_{-\infty}^{+\infty} d\nu\ |\nu| \times e^{-2i\pi\nu(u - x\cos\varphi - y\sin\varphi)} g(u,\varphi) \qquad (19)$$

Equation (19) is called Filtered Back-Projection method (FBP). In this case the FBP is an exact inversion formula obtained by combining the action of the ramp filter and the back-projection operation of the Radon transform. This is the most popular inversion method for the ordinary Radon transform due to its rapid algorithmic implementation.

In our case, we propose an empirical FBP for the inversion procedure of CART, but instead of working with straight lines,we use circular-arcs. The implementation of the circular-arc FBP is carried out as follows. The reconstruction can be written as

$$\tilde{f}(r,\theta) = \int_0^{2\pi} d\varphi \int_0^{\frac{\pi}{2}} d\omega\ g(\varphi,\omega) \times \delta\left[r - p\left(\sqrt{1 + \frac{\cos^2(\theta-\varphi)}{\tan^2\omega}} - \frac{\cos(\theta-\varphi)}{\tan\omega}\right)\right]. \qquad (20)$$

We can rewrite this formula using the equation (15):

$$\tilde{f}(r,\theta) = \int_0^{2\pi} \frac{d\varphi}{|J((\theta-\varphi),r,p)|} \times g\left(\varphi, \arctan\left(\frac{2pr}{p^2-r^2}\cos(\theta-\varphi)\right)\right), \qquad (21)$$

where

$$J((\theta-\varphi),r,p) = \frac{r}{\cos(\theta-\varphi)}\frac{2rp}{p^2+r^2} \times \left\{\left(\frac{p^2+r^2}{2pr}\right)^2 - \sin^2(\theta-\varphi)\right\}. \qquad (22)$$

In order to reduce the artifacts, we apply a "Hann" filter on the data before using equation (20 or 21) for image reconstruction.

Numerically this equation means that we give every point on the circular-arc $C(\varphi,\omega)$ the value $g(\varphi,\omega)$ and sum over the contributions of all projections $g(\varphi,\omega)$.

Fig. 7 shows the principle of Back-Projection for two angles φ and three angles ω. After acquisition, Back-Projection corresponds to a data spreading in the medium. So each point, belonging to one of the circular-arc $C(\varphi_i,\omega_j)$, receives the corresponding value $g(\varphi_i,\omega_j)$ and the intersection points between $C(\varphi_i,\omega_j)$ and $C(\varphi_{i'},\omega_{j'})$ receive the sum $g(\varphi_i,\omega_j) + g(\varphi_{i'},\omega_{j'})$.

It is well-known that the FBP leads to the artifacts because of the limited number of projections (data). The smaller is the discretization step, the better is the image quality. But in the case of circular-arc FBP there are problems due to the geometrical nature of the circular arcs. They intersect at two points (Fig. 7) whereas straight lines in the classical Radon transform intersect only at one point. It is difficult to locate the scattering site. However with enough data (projections), this problem is not so important.

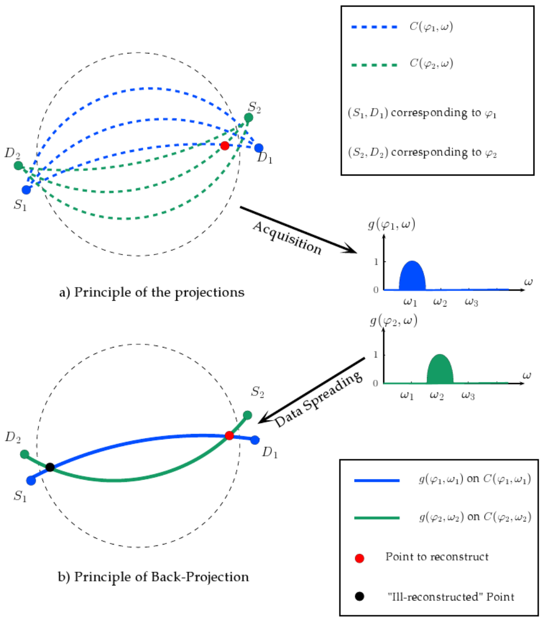

Fig. 7 Principle of Back-Projection

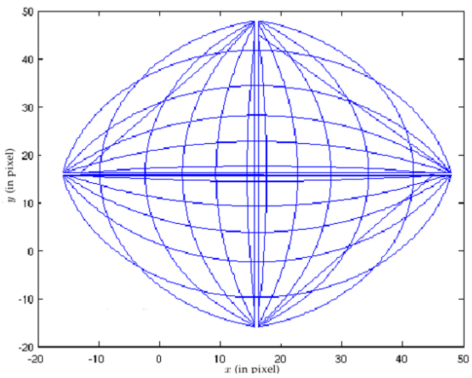

Fig. 8 Intersection distribution

Another difficulty comes from the heterogeneous distribution of these intersections. Fig. 8 shows their distribution and we can see a concentration of the intersections at the center of the medium. This implies an over-estimation of this area when the FBP is applied. Indeed these points will receive a higher value during the FBP because they correspond to many more projections. This phenomenon yields a false estimation around the proximity of the center.

3.4 Simulation results

In this section, we present the simulation results of the CART and compare the reconstructions obtained by the CART, by the Radon transform Filtered Back-Projection (RT FBP) and by the Norton Radon transform Filtered Back-Projection (NRT FBP). Indeed for the Norton case, we use the FBP method proposed by Norton [9].

To compare the quality of the reconstructions, we define the Mean Squared Error (MSE) and the Mean Absolute Error(MAE):

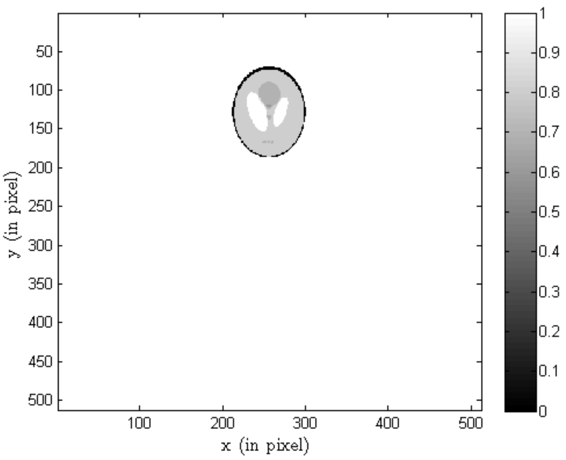

Fig. 9 Original Shepp-Logan phantom

$$MSE = \frac{\|I_r - I_o\|_2^2}{N^2} \tag{23}$$

$$MAE = \frac{\|I_r - I_o\|_1}{N^2} \tag{24}$$

where I_r is the reconstructed image and I_o is the original image.

We present first the results of numerical simulations for a point object with $d\varphi = 1^o$ and with 300 energy levels. The original image is in Fig. 5, its projection in Fig. 12 and its reconstruction in Fig. 15. The artifacts are observed in the center region as discussed above. Despite these artifacts, the structure of the point object is clearly reconstructed. We can compare this reconstruction with the reconstructions obtained by the Radon transform FBP (Fig. 13) and by the Norton Radon transform FBP (Fig. 14). The Mean Squared Error (MSE) and the Mean Absolute Error (MAE) quantify the quality of the reconstruction and the results show that the proposed CART FBP gives a reconstruction quality equivalent to that of the Radon transform and better than the Norton Radon transform's one (Tab. 1).

Then the Shepp-Logan medical phantom (Fig. 9) of size 128×128 in a medium of size 512×512 is simulated. Indeed because of the distribution of the artifacts, we cannot reconstruct an object placed in the center area. We take $d\varphi = 1^o$ and 800 energy levels in order to keep the conditioning of the system ($N_\varphi \times N_\omega \geq N^2$).

Fig. 18 shows the CAR transform of the phantom which is the image of Compton scattered radiation on the camera. The reconstructions using FBP are given in Fig. 21. Figs. (16,17) show the Radon transform and the Norton Radon transform of the same phantom. Figs. (19,20) give the reconstructions using RT FBP and NRT FBP. As above mentioned the artifacts are observed in the center region. However the calculated errors (Tab. 2) prove that the reconstruction quality by the CART is similar to the one obtained by the Radon transform but better than the one obtained by the Norton procedure.

Moreover the small structures in the object are clearly reconstructed. This result illustrates undoubtedly the feasibility of this new imaging modality.

We obtain the following results :

Tab. 1 "MSE and MAE of different reconstructions of the point object in Fig. 5"

Method	MSE	MAE
RT	2.1×10^{-5}	0.0015
NRT	2.65×10^{-4}	0.0053
$CART$	6.3×10^{-6}	0.001

Tab. 2 "MSE and MAE of different reconstructions of the Shepp-Logan phantom with a zoom in Fig. 9"

Method	MSE	MAE
RT	3.5×10^{-4}	0.0233
NRT	0.0021	0.0808
$CART$	0.0013	0.0532

4 Conclusion and perspectives

A new Compton scattering tomography is shown feasible due to modeling and simulations with help of a novel circular-arc Radon transform. The simulation of the analytical inversion formula is our current work.

In this new imaging, studied matter is characterized by its electron density (scattering sites), which has the advantage of being less sensitive to matter aging than its attenuation coefficient used in X-ray scanning tomography. The CAR transform solves the Compton scattering problem which remains a major technical challenge until now (scattered photons cause blurs, loss of contrast of image and false detections). Moreover the new CST proposes an alternative to the current tomographies keeping the quality of reconstruction. Transmission Compton tomography can be combined with emission Compton tomography to form a new bimodal imaging process based on scattered radiation. Modeling and simulation of the last one may be the subject of future investigations.

5 References

[1] M.K. Nguyen and T.T. Truong. On an integral transform and its inverse in nuclear imaging. *Inverse Problems*, 18:265–277, 2002.

[2] M.K. Nguyen T.T. Truong, J.L. Delarbre and N. Kitanine. Three dimensional object reconstruction from compton scattered gamma ray data. In Milan Sonka Ioannis Kakadiaris and Jan Kybic, editors, *Computer vision and mathematical methods in medical and bio-medical image analysis*, pages 24–34, Springer Verlag, Heidelberg, 2004.

[3] M.K. Nguyen T.T. Truong, H.H. Bui and J.L. Delarbre. A novel inverse problem in gamma-ray emission imaging. *Journal of Inverse Problems in Science and Engineering*, 12:225–246, 2004.

[4] J.L. Delarbre M.K. Nguyen, T.T. Truong and J.L. Starck. Modeling and simulation for scattered gamma-ray imaging. In *Proc. 5th EUROSIM Congress on Modeling and Simulation*, Marne la Valle, France, September 2004.

[5] C. Driol M.K. Nguyen and T.T. Truong. Modeling and simulation results on high sensitivity scattered gamma-ray imaging. In *Proc. 6th EUROSIM Congress on Modeling and Simulation*, September 2007.

[6] E.M.A. Hussein D.A. Meneley and S. Banerjee. On the solution of the inverse problem of radiation scattering imaging. *Nuclear Science and Engineering*, 92:341–349, 1986.

[7] N.V. Arendtsz and E.M.A. Hussein. Energy-spectral compton scatter imaging - part 1: theory and mathematics. *IEEE Transactions on Nuclear Sciences*, 42:2155–2165, 1995.

[8] R. Guzzardi and G. Licitra. A critical review of compton imaging. *CRC Critical Reviews in Biomedical Imaging*, 15:237–268, 1988.

[9] S.J. Norton. Compton scattering tomography. *Jour. Appl. Phys.*, 76:2007–2015, 1994.

[10] A.M. Cormack. Radon's problem - old and new. *SIAM-AMS Proceedings*, 14:33–39, 1984.

[11] M.K. Nguyen and T.T. Truong. Inversion of a new circular-arc radon transform for compton tomography. *Inverse Problems*, 26:065005(13pp), 2010.

[12] M.K. Nguyen T.T. Truong, Clemence Driol and Habib Zaidi. On a novel approach to compton scattered emission imaging. *IEEE transactions on nuclear science*, 56:1430–1437, June 2009.

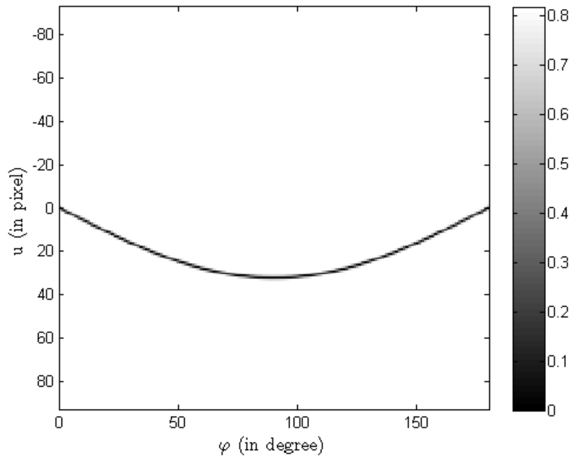

Fig. 10 Radon transform of the point object in Fig. 5 ($g(u, \varphi)$ of eq.(17))

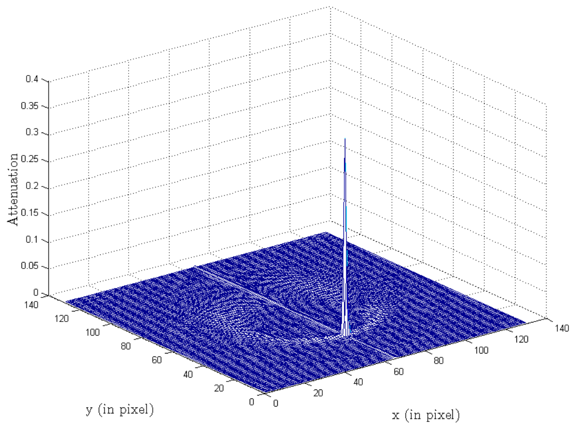

Fig. 13 Reconstruction of the point object in Fig. 5 by RT FBP ($f(x, y)$ of eq. (19))

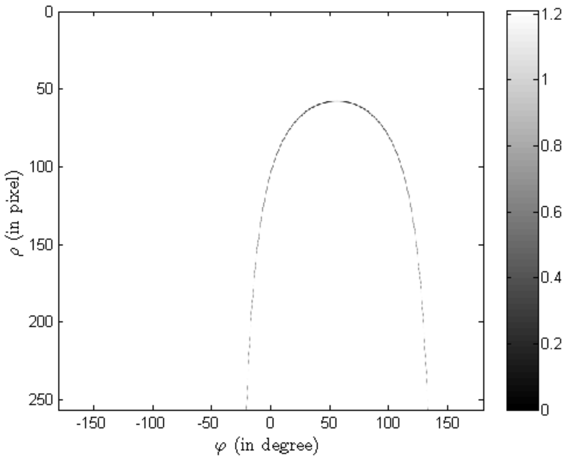

Fig. 11 Norton Radon transform of the point object in Fig. 5 ($g(\rho, \varphi)$ of eq. (2))

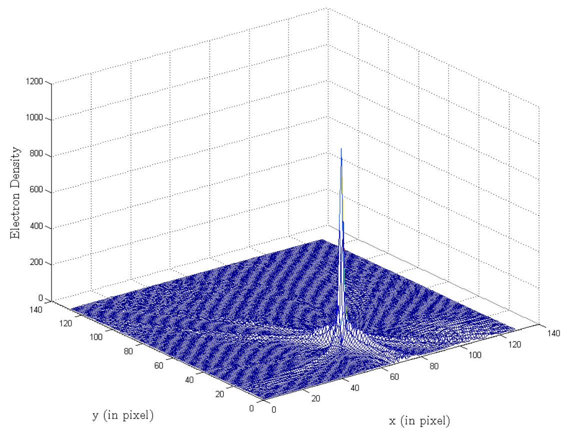

Fig. 14 Reconstruction of the point object in Fig. 5 by Norton RT FBP ($f(r, \theta)$ of eq. (4))

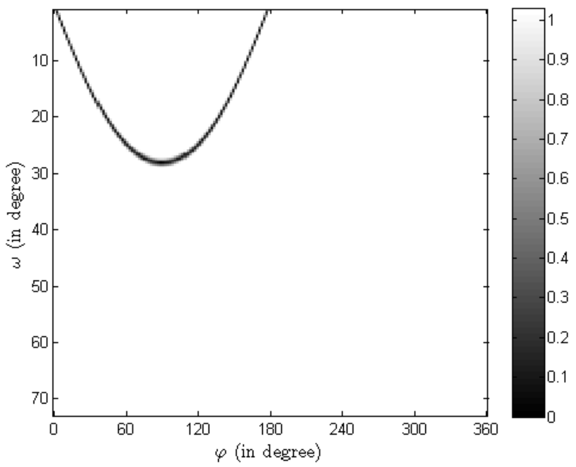

Fig. 12 CAR transform of the point object in Fig. 5 ($g(\varphi, \omega)$ of eq. (9))

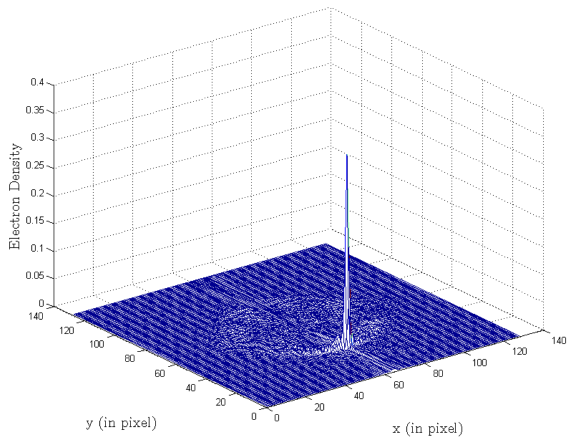

Fig. 15 Reconstruction of the point object in Fig. 5 by CART FBP ($\tilde{f}(r, \theta)$ of eq. (20))

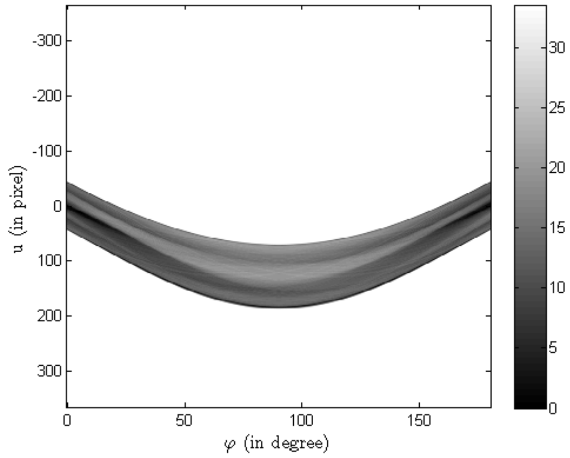

Fig. 16 Radon transform of the phantom in Fig. 9 ($g(u, \varphi)$ of eq. (17))

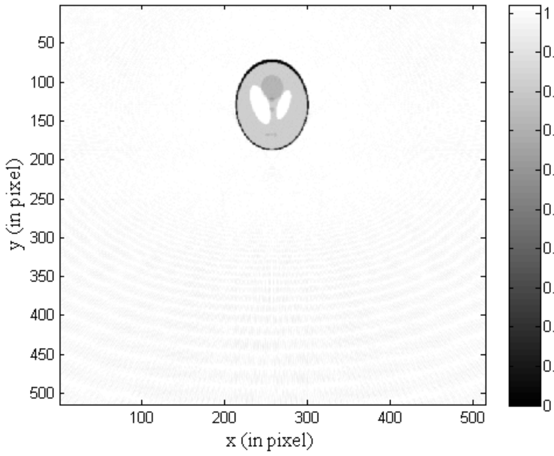

Fig. 19 Reconstruction of the phantom in Fig. 9 by RT FBP ($f(x, y)$ of eq. (19))

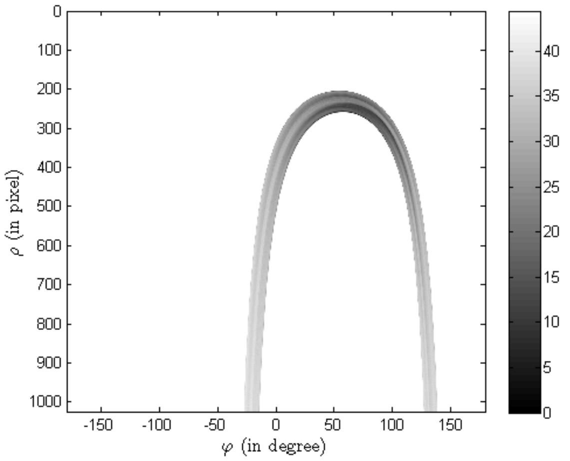

Fig. 17 Norton Radon transform of the phantom in Fig. 9 ($g(\rho, \varphi)$ of eq. (2))

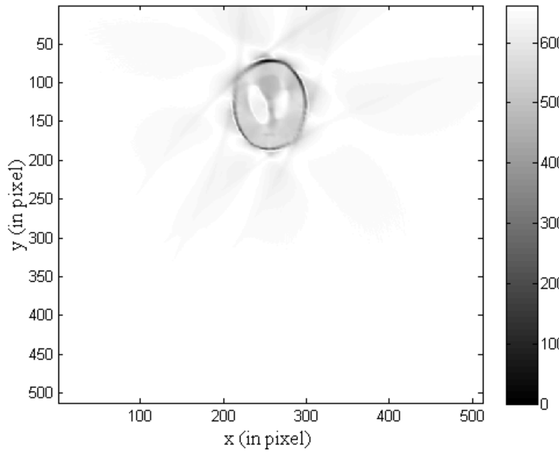

Fig. 20 Reconstruction of the phantom in Fig. 9 by Norton RT FBP ($f(r, \theta)$ of eq. (4))

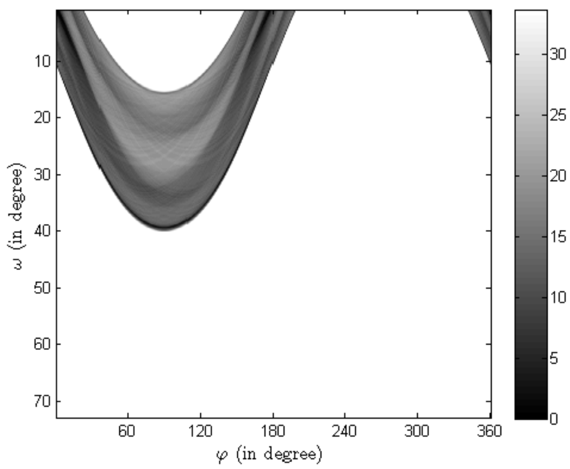

Fig. 18 CAR transform of the phantom in Fig. 9 ($g(\varphi, \omega)$ of eq. (9))

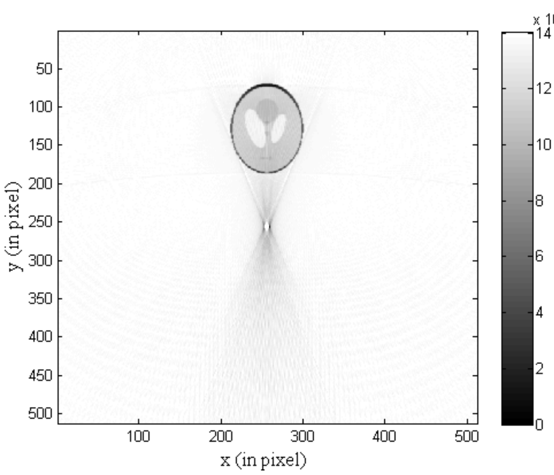

Fig. 21 Reconstruction of the phantom in Fig. 9 by CART FBP ($\tilde{f}(r, \theta)$ of eq. (20))